Mechanisms of explosive volcanism on Mercury: implications from its global distribution and morphology

AGU PUBLICATIONS

JGR

Journal of Geophysical Research: Planets

RESEARCH ARTICLE
10.1002/2014JE004692

Key Points:
- One hundred fifty candidate sites of explosive volcanism identified on Mercury
- Regional and local distribution support a structural control on eruption
- Probable concentration of volatiles during shallow magma storage

Supporting Information:
- Readme
- Figure S1
- Figure S2
- Figure S3
- Figure S4
- Table S1
- Table S2
- Table S3
- Table S4

Correspondence to:
R. J. Thomas,
Rebecca.Thomas@open.ac.uk

Citation:
Thomas, R. J., D. A. Rothery, S. J. Conway, and M. Anand (2014), Mechanisms of explosive volcanism on Mercury: Implications from its global distribution and morphology, *J. Geophys. Res. Planets*, *119*, 2239–2254, doi:10.1002/2014JE004692.

Received 11 JUL 2014
Accepted 30 SEP 2014
Accepted article online 3 OCT 2014
Published online 27 OCT 2014
Corrected 27 FEB 2015

This article was corrected on 27 FEB 2015. See the end of the full text for details.

Mechanisms of explosive volcanism on Mercury: Implications from its global distribution and morphology

Rebecca J. Thomas[1], David A. Rothery[1], Susan J. Conway[1], and Mahesh Anand[1,2]

[1]Department of Physical Sciences, Open University, Milton Keynes, UK, [2]Department of Earth Sciences, Natural History Museum, London, UK

Abstract The identification of widespread pyroclastic vents and deposits on Mercury has important implications for the planet's bulk volatile content and thermal evolution. However, the significance of pyroclastic volcanism for Mercury depends on the mechanisms by which the eruptions occurred. Using images acquired by the MErcury Surface, Space ENvironment, GEochemistry, and Ranging spacecraft, we have identified 150 sites where endogenic pits are surrounded by a relatively bright and red diffuse-edged spectral anomaly, a configuration previously used to identify sites of explosive volcanism. We find that these sites cluster at the margins of impact basins and along regional tectonic structural trends. Locally, pits and deposits are usually associated with zones of weakness within impact craters and/or with the surface expressions of individual thrust faults. Additionally, we use images and stereo-derived topographic data to show that pyroclastic deposits are dispersed up to 130 km from their source vent and commonly have either no relief or low circumpit relief within a wider, thinner deposit. These eruptions were therefore likely driven by a relatively high concentration of volatiles, consistent with volatile concentration in a shallow magma chamber prior to eruption. The colocation of sites of explosive volcanism with near-surface faults and crater-related fractures is likely a result of such structures acting as conduits for volatile and/or magma release from shallow reservoirs, with volatile overpressure in these reservoirs a key trigger for eruption in at least some cases. Our findings suggest that widespread, long-lived explosive volcanism on Mercury has been facilitated by the interplay between impact cratering, tectonic structures, and magmatic fractionation.

1. Introduction

Traditional models of Mercury's formation predict a volatile-depleted bulk composition [*Cameron*, 1985; *Fegley and Cameron*, 1987; *Wetherill*, 1988; *Benz et al*., 2007]. Therefore, evidence for widespread explosive, volatile-driven volcanism on the innermost planet in the solar system was not anticipated prior to the arrival of the MErcury Surface, Space ENvironment, GEochemistry, and Ranging (MESSENGER) spacecraft. However, images from MESSENGER flybys showed irregular, apparently endogenic pits surrounded by deposits that are spectrally bright and red relative to the Hermean average. The anomalous spectral character of the deposits, their association with a central depression, and their diffuse outer margins all support their emplacement by explosive volcanism [*Head et al*., 2008; *Kerber et al*., 2009]. Under the airless conditions at Mercury's surface, this emplacement would have occurred by ejection of pyroclasts along ballistic trajectories. *Kerber et al*. [2009, 2011] and *Goudge et al*. [2014] used MESSENGER flyby and orbital images to produce a catalogue of 51 pyroclastic deposits. The current study increases this number, finding 150 sites, at many of which there are multiple pits and deposits. The spatial extent of the deposits has been used to calculate that their formation by steady fire fountaining would require a high magma volatile content [*Kerber et al*., 2011], further challenging the expectation that Mercury is volatile depleted. However, to infer the magma volatile content powering an explosive eruption, it is necessary to determine the mechanisms by which eruption occurred: if magma rise were slow or stalled below the surface, volatiles could become concentrated prior to an eruption and so they would not reflect the volatile content of the magma at source. To understand the intrinsic volatile content of Hermean magmas and of the planet as a whole, it is therefore important to constrain the mechanisms by which explosive eruptions occurred on Mercury.

A further surprising feature of Mercury's explosive volcanism is its global longevity. We have shown elsewhere [*Thomas et al*., 2014b] that explosive volcanic eruptions occurred over a long period from 3.8 Ga to

as recently as 1 Ga. Large-scale thrust faults attest to considerable crustal shortening at the beginning of this period [*Strom et al*., 1975], and thrust faults that crosscut young craters show that this state of compression has persisted until geologically recently (and may still prevail today) [*Banks et al*., 2014]. This stress regime would tend to impede dike propagation and so inhibit eruption of magma at the surface. Additionally, if Mercury initially contained the same proportion of heat-producing elements as larger terrestrial planets like Earth, it would have cooled, and its lithosphere thickened, more quickly due to its higher surface-area-to-volume ratio. Both of these conditions mean that volcanism should be hampered late in the planet's history, in conflict with the observations. Hence, further investigation is required to elucidate the mechanisms that permit late-stage Hermean volcanism.

Previous studies have identified sites of explosive volcanism on Mercury by searching for spectrally distinct, relatively bright and red surface deposits, and then noting whether a vent occurs within those deposits [*Kerber et al*., 2011; *Goudge et al*., 2014]. Here we take a different approach by examining MESSENGER images first for probable endogenic pits and then for bright, red surrounding deposits. This method allows us to increase threefold the number of published candidate sites for explosive volcanism and thus to better understand their overall distribution. With the aid of stereo-derived digital elevation models (DEMs) and Mercury Laser Altimeter (MLA) data, we investigate the 3-D topography of the pits and deposits, and we combine this with their spatial distribution to better constrain the eruption mechanisms responsible for Mercury's widespread, long-lived explosive volcanism.

2. Methods

2.1. Identifying Sites of Explosive Volcanism

To identify endogenic pits and surrounding deposits, we examined images taken by MESSENGER's Mercury Dual Imaging System (MDIS) [*Hawkins et al*., 2007] prior to 17 March 2013. We first identified pits in monochrome images and then examined color images to determine whether those pits were surrounded by spectrally distinctive (i.e., bright and red) deposits.

2.1.1. Pits

As part of an earlier study [*Thomas et al*., 2014a] we surveyed all MESSENGER narrow angle camera (NAC) and wide angle camera (WAC) images at a resolution of 180 m/pixel or better, noting all endogenic depressions. These depressions were numbered using an arbitrary scheme, with numbers ranging from 1000 to 8999. We distinguished such depressions from impact craters (exogenic depressions) on the basis of their departure from planform circularity and the absence of the characteristic ejecta deposits, terraces, raised rim, and central uplifts of impact craters. We applied radiometric and photometric corrections to these images using ISIS 3 image processing software produced by the U.S. Geological Survey. We also examined the Planetary Data System (PDS)-hosted 250 m/pixel global monochrome mosaic (March 2013 release) to ensure that no large-scale depressions, not otherwise visible with individual NAC and WAC frames, had been missed.

We classified all subsequently identified depressions as either pits, hollows, or pitted ground (Figure 1). Pits are the deepest type of depression and generally have sloping floors. Any surrounding spectral anomaly is redder than the Hermean average. Hollows can individually be as little as tens of meters across, are shallow and flat floored, and have steep margins [*Blewett et al*., 2011]. They are floored and haloed by relatively bright and blue deposits and probably form largely by sublimation or some other nonexplosive process [*Thomas et al*., 2014a] and so are not considered further in this study. Pitted ground is morphologically intermediate between pits and hollows: it consists of an area of the surface with an uneven, pitted appearance of a similar to somewhat greater depth than hollows but with a more rounded texture. In some cases pitted ground is surrounded by a steep margin. Where floored and surrounded by spectrally bright and red deposits, it is probable that, like pits, this type of depression has a volcanic genesis. *Thomas et al*. [2014a] suggested that pitted ground forms when volatile escape disturbs an overlying stratum such as cooling lava, rather than by vent-centered explosive volcanism. On that basis, pitted ground has also been excluded from further investigation in this study.

We digitized the margin of each pit on the global monochrome mosaic using ArcGIS software and noted its location and geodetic areal extent using Tools for Graphics and Shapes software [*Jenness*, 2011]. Where a pit lay within an impact crater or its proximal ejecta blanket, we noted its specific location in the crater (i.e., crater wall, peak structure, smooth or rough floor, or proximal ejecta). Where several

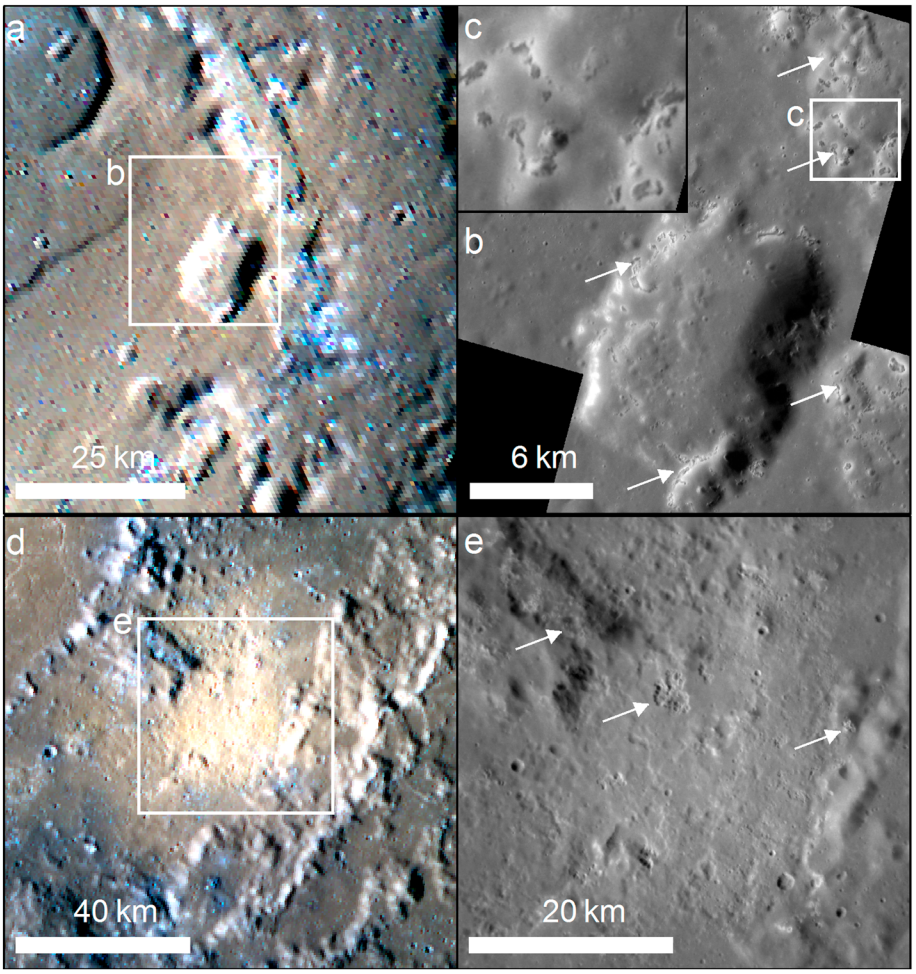

Figure 1. Types of depression on Mercury: pits, pitted ground, and hollows. (a) Peak ring area of Praxiteles crater (−59.1°E, 26.9°N) with both a pit with surrounding bright, red deposits and hollows with bright, blue deposits. White square: extent of Figure 1b. (Color composite of frames EW0253964972I, EW0253964964G, and EW0253964968F). (b) Close-up of the pit and surrounding hollows. The pit is larger and has a rounded floor, while the hollows are smaller, have flat floors, and occur in clusters. Square: extent of Figure 1c. Arrows: clusters of hollows (images EN0223701867M and EN0223701860M). (c) Close-up of hollows showing their fresh morphology, steep margins, and flat floors (image EN0223701860M). (d) Pitted ground: a bright, red deposit on the floor of Rachmaninoff crater (59.6°E, 26.1°N) with bright, blue deposits (hollows) on the peak ring and terraces around it. Square: extent of Figure 1e (composite of EW0254942272I, EW0254942264G, and EW0254942268F). (e) Close-up showing the uneven, subtly pitted surface of the bright, red area (pitted ground) and hollows (white arrows) superposing and around it (image EN0224338598M).

pits were identified within an impact crater or clustered within 50 km of each other (an arbitrarily defined distance), they were grouped into a single site. Where a pit lies within 20 km of a lobate scarp or wrinkle ridge, or incises a crater that is affected by or overlies such tectonic structures, we noted this association. The surface traces of these tectonic structures were identified by reference to the 1:2,000,000 scale global fault map of *Byrne et al.* [2014], complemented by examination of high-resolution NAC data and our topographic products (see section 2.2).

2.1.2. Deposits and Substrates

To identify spectrally distinct deposits around pits, we constructed color images by combining images from 996 nm, 749 nm, and 433 nm WAC filters in the red, blue, and green channels, respectively. This combination of wavelengths was chosen because such images allow for robust identification of spectral variations on Mercury's surface despite its generally red sloped reflectance spectrum [*Denevi et al.*, 2009]. We created and examined color composites for all images at a resolution of 1000 m/pixel or better and also examined the PDS-hosted 1000 m/pixel global color mosaic (March 2014 release).

We digitized the extent of each identified spectral anomaly and calculated its area as for pits. This areal value should be viewed as a minimum because the margins of these anomalies are diffuse and we took a conservative approach to judging their limit, excluding the more tenuous outer fringe. Additionally, it is likely that the present visible area of a given deposit is less than its original extent due to averaging of the observed surface spectrum by impact gardening and, depending on composition, by space weathering. Modification of spectra by these effects will become more pronounced over time.

2.2. Investigating Topography

2.2.1. Data Acquisition

Where available, we used Mercury Laser Altimeter (MLA) [*Cavanaugh et al*., 2007] data to characterize the topography of the pits and deposits. The along-track spacing of data points is ~400 m at all latitudes, but the horizontal footprint and between-track spacing are both at a minimum at periapsis (~60°N). No MLA data are available for the region south of ~5°S.

Where a MLA track directly crosses a pit or its deposits, we constructed a topographical cross section along it. Where many tracks are available in close proximity to the pit, we constructed a digital elevation model (DEM) using natural neighbor interpolation using ArcGIS, in a sinusoidal projection centered on the pit.

For those pits not crossed by MLA tracks, we used stereo images (NAC or WAC frames using the 750 nm filter) to create high-resolution DEMs by photogrammetry using the Ames Stereo Pipeline (ASP) [*Moratto et al*., 2010]. Where possible, we used MLA points to vertically control the DEM. Because it is difficult for ASP to identify single-pixel correspondences between two images, point data were averaged on a 3×3 block of pixels, giving the DEM a resolution 3 times lower than the images from which is was derived. The resulting DEMs range in resolution from 215 to 880 m/pixel. In some cases, the stereo-derived DEMs had a monotonic slope across the scene. For stereo-derived DEMs without MLA control this slope may be an artifact of stereo correlation. In other cases, however, such a slope is a geological reality, as where regional tilting due to long-wavelength warping has been observed at numerous sites across Mercury [*Zuber et al*., 2012; *Byrne et al*., 2014]. If a tilt was judged to be an artifact, or interpreted as real on the basis of its regional context but to have occurred after pit formation, we applied a linear detrending to the DEM using ArcGIS. Where the pit lay within a flat-floored impact crater, the dip of that floor (which can be assumed to have been originally horizontal) was used to judge the trend. In other cases, the dip of the entire DEM was used for this purpose.

Where possible, we calculated pit volume from a DEM by interpolating an additional surface above the pit on the basis of the topography in a buffer beyond its rim and calculating the volume difference between these two surfaces using the Cut Fill tool in ArcGIS. Where the unevenness of the surrounding surface or anomalous values in shadowed areas of the DEM made this approach impractical, we calculated pit volume by determining pit depth from our topographic data, measuring length and width in planform in a sinusoidal projection centered on the pit, and then calculating the volume by approximating it to a hemiellipsoid, cone, or trench, depending on the pit morphology. To calculate the slopes of circumpit deposits and of pit walls, we calculated the gradient between the DEM pixel values or MLA points at the slope top and base.

2.2.2. Data Accuracy and Error

The potential for horizontal and vertical error varies between the data types. MLA data have a vertical accuracy with respect to Mercury's center of mass of < 20 m and a range precision of < 1 m under nadir-viewing conditions. The horizontal accuracy of MLA data depends on the accuracy of the spacecraft pointing data but can be approximated as being of the order of the footprint size, which varies from 15 to 100 m, peaking at apoapsis.

The error in stereo-derived DEMs produced using ASP is more difficult to quantify. To explore this issue, we constructed a DEM with and without MLA control at five sites. Both DEMs were detrended, and the mean elevation difference and the difference in horizontal scale were calculated. We found that horizontal differences are negligible (<1%), but vertical differences are considerable: the standard deviation in relative elevation difference ranges from 42 to 79 m.

We calculated the error on our slope measurements by obtaining the slope of a best fit line through MLA points and through raster pixels in the MLA-controlled and uncontrolled DEMs along cross sections at 10

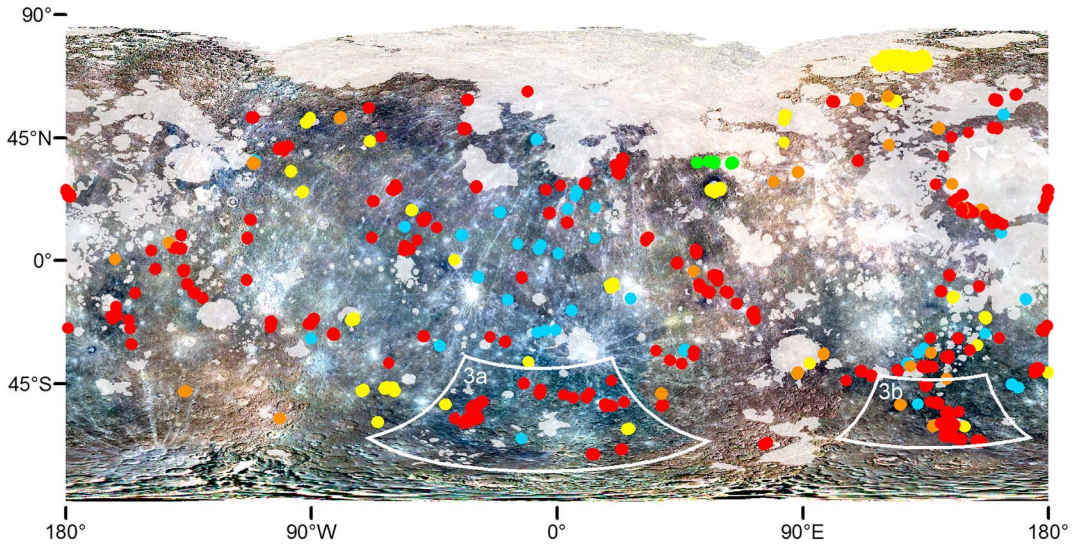

Figure 2. Distribution of endogenic pits and areas of spectrally red pitted ground. Red dots: endogenic pits with an associated bright, red spectral anomaly. Orange dots: endogenic pits without a visible spectral anomaly. Yellow dots: spectrally red pitted ground. Blue dots: sites where pits or deposits indicate possible (but not definitive) explosive volcanism. Green dots: aligned endogenic pits between Rachmaninoff basin and smooth plains. White boxes: locations of Figures 3a and 3b. White areas: mapped smooth volcanic plains [*Denevi et al*., 2013]. (Base image: global color MDIS mosaic version 5.).

locations across the five test cases. The mean slope difference between MLA-controlled DEMs and MLA profiles is 3%, whereas it is 13% between uncontrolled DEMs and MLA data.

2.2.3. Identification of Deposits

Because both tectonic and impact processes can produce substantial topography, care was taken to interpret all anomalous topography near endogenic pits on the basis of planform imagery and to attribute it to volcanic deposition only where no other explanation was viable. Where a pit covers a large proportion of an impact crater floor, topography resulting from pyroclastic deposition cannot be distinguished from that of the impact crater's original terrace/wall, and where pits occur outside an impact crater on rough terrain, only thick deposits with clear circumpit topographic expression can be identified other than by color. Therefore, topography owing to volcanic deposition may not have been recognized at all locations where it is present, and we have most commonly identified such topography on the otherwise smooth, flat floors of impact craters.

3. Results

3.1. Occurrence of Endogenic Pits and Deposits

We identified 174 candidate endogenic pit sites, at 150 of which a bright and red spectral anomaly is visible (Figure 2). There are multiple pits at 64 of these sites, with a total of 327 pits overall (Table S1 in the supporting information). Previous to this work, the largest number of putative pyroclastic deposits identified on Mercury was 137 [*Kerber et al*., 2014], of which 51 had been identified in earlier published studies [*Kerber et al*., 2011; *Goudge et al*., 2014]. Our study finds 57 additional deposit locations not identified in *Kerber et al*. [2014]. We do not observe an endogenic pit with an associated deposit at 40 of their candidate locations, but we do identify spectrally red pitted ground at 15 of those 40 locations and an endogenic pit lacking a surrounding deposit at two.

3.1.1. Global and Regional Distribution

Endogenic pits are widespread on Mercury, although they are rare (only 5 of the 327 individual pits) on thick high-reflectance volcanic plains such as those at high northern latitudes and inward of the margins of the fill within the Caloris impact basin (Figure 2). Pits are not randomly distributed: the 327 individual pits have an average Nearest Neighbor ratio of 0.402, indicating that they are on average separated by less than half the distance expected in a random distribution. Additionally, pits have a Moran's Index of 0.148 based on

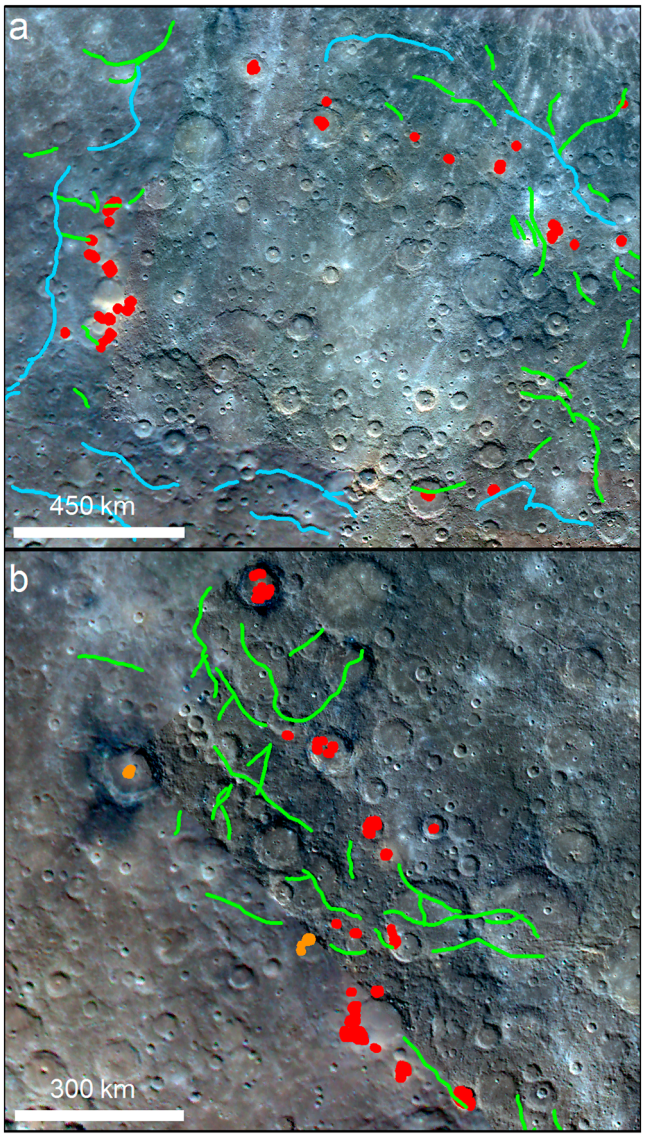

Figure 3. Regional alignments of endogenic pits and their association with tectonic structures. (a) Alignments of pits with a surrounding bright, red spectral anomaly at the margins of a subcircular area bounded by faulting. Red dots: pits with spectrally bright, red deposits. Blue lines and green lines: high-terrain-bounding structures and cratered plain structures [after *Byrne et al*., 2014]. (Global MDIS color mosaic v5, Lambert equal area projection centered on −6°E, −57°N). (b) Alignment of endogenic pits with and without (red and orange dots, respectively) a surrounding spectral anomaly that lies along a faulted, heavily cratered region. The colored lines and base map image are as for Figure 3a, with projection centered on 137°E, −46°N.

their areal extent, a result indicating that those with a similar planform area are clustered. This statistic measures correlation in a value between different locations [*Moran*, 1950]; a value of −0.003 indicates no spatial correlation between pits of a similar size. For both statistics, the *z* value indicates a likelihood of less than 1% that this clustering is the result of random chance.

Clustering of pits is especially apparent at the margins of large impact basins. As previously noted [*Head et al*., 2008; *Goudge et al*., 2014; *Rothery et al*., 2014], many endogenic pits and deposits occur around the marginal fill and rim of the Caloris Basin. Our study also finds conspicuous alignments of pits with spectrally distinct deposits around a proposed ancient impact basin, listed as "b54" by *Fassett et al*. [2012], located in the southern hemisphere at approximately −2°E, −59°N (Figure 3a). The pits form alignments at the north and west of a relatively smooth unit that may correspond to volcanic infill within the basin. The region is surrounded by contractional tectonic structures [*Byrne et al*., 2014], many of which bound high-standing terrain just outside the zone where the pits occur. Although this putative basin is heavily degraded and therefore very old, some of the pits surrounding it are much more recent: for example, the westernmost pit in this area incises the 27 km diameter Kuniyoshi crater, which appears to be Kuiperian (< 1 Ga) or at least Late Mansurian (1.7–1 Ga) [*Thomas et al*., 2014b].

There is also evidence that pits occur along regional tectonic trends that appear unrelated to basin structures. For example, in another area in the southern hemisphere at 137°E, −46°N (Figure 3b), endogenic pits with and without bright, red deposits occur in a relatively high standing, extensively faulted region. These pits have the same general trend as, but are not collocated with, the largest faults.

3.1.2. Local Associations

At 81% of the candidate pit sites, and 79% of those with a bright, red spectral anomaly, pits occur within an impact crater. The pits tend to occur at sites within the crater where there may be a structural control on their formation, such as at or around central uplift structures and along wall terraces. As noted above, pits

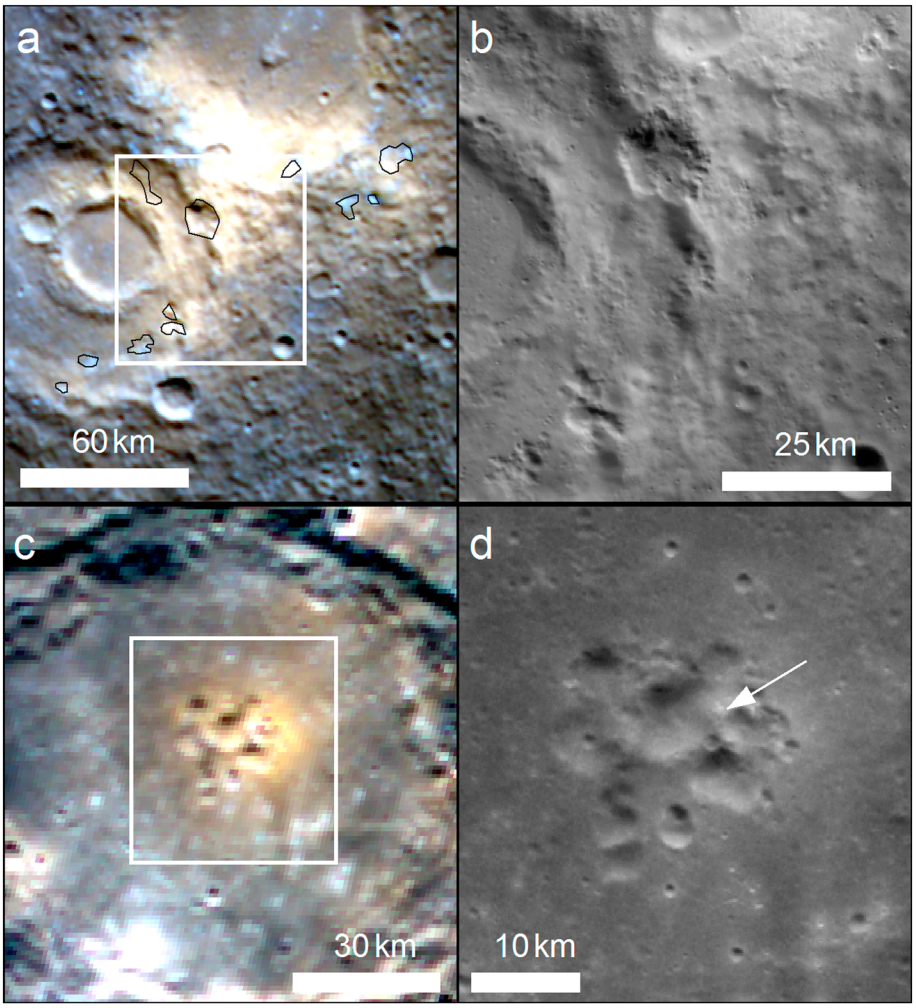

Figure 4. Examples of multiple pits at a single location surrounded by relatively bright, red deposits indicating a complex history of volcanism. The white square in Figures 4a and 4c indicates the extent of Figures 4b and 4d. (a) Many pits (outlined in black) occur over an area within and between two craters (−31.9°E, −58.1°N) and are surrounded by a bright, red spectral anomaly. Activity may have occurred concurrently or sequentially from different vents (composite of frames EW1005108006I, EW1005108026G, and EW1005108010F). (b) Close-up showing that some of the pits in Figure 4a are similarly pristine (image EN0239040293M). (c) Multiple small pits around the center of an impact crater at −6.5°E, −48.4°N. The spectral anomaly is brightest around the northeast pits (composite of EW0222840754I, EW0222840774G, and EW0222840758F). (d) Close-up of Figure 4c showing that the pits at the center of the brightest deposits have the freshest morphology and incise into the margins of the pits to their north (white arrow) and west, indicating that they postdate them (image EN0253479661M).

also occur in association with tectonic structures: at 46% of pit sites and 47% of those with bright, red deposits they occur in close proximity to one or more surface fault traces. These tectonic structures are in all cases lobate scarps or wrinkle ridges, which are thought to be the surface expressions of thrust faults [*Schultz*, 2000; *Watters et al.*, 2009]. In total, pits occur either in association with the surface trace of a thrust fault or within an impact crater at 92% of pit sites where there are associated bright, red deposits. Additionally, at some sites pit alignment suggests a subsurface structural control, such as where pits occur radial to the center of Caloris [*Rothery et al.*, 2014] or where four pits form a 550 km long line between the Rachmaninoff basin and the southern edge of the northern plains (at 50 −67°E, 36°N; green dots in Figure 2).

Although endogenic pits are rare or absent in the central part of volcanic plains, where plains thickness is expected to be greatest, evidence for explosive volcanism is frequently present at locations where it is probable that effusive volcanism preceded it: 30% of endogenic pits with a surrounding spectral anomaly occur within probable lavas. For example, pits incise the floors of impact craters that are of a diameter where

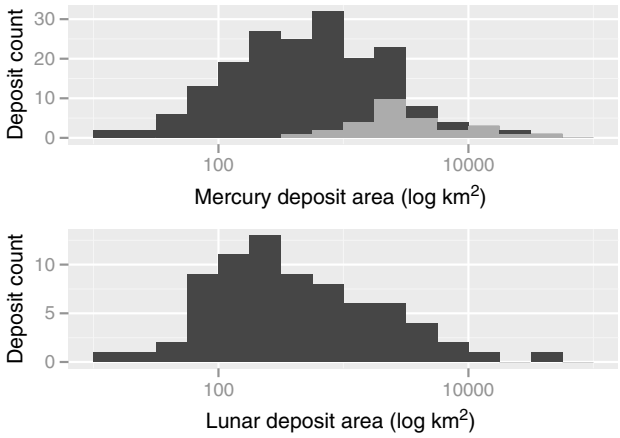

Figure 5. Comparison of the size of pyroclastic deposits on (a) Mercury (light gray: documented by *Kerber et al*. [2011] and dark gray: this study) with (b) those on the Moon [*Gaddis et al*., 2003].

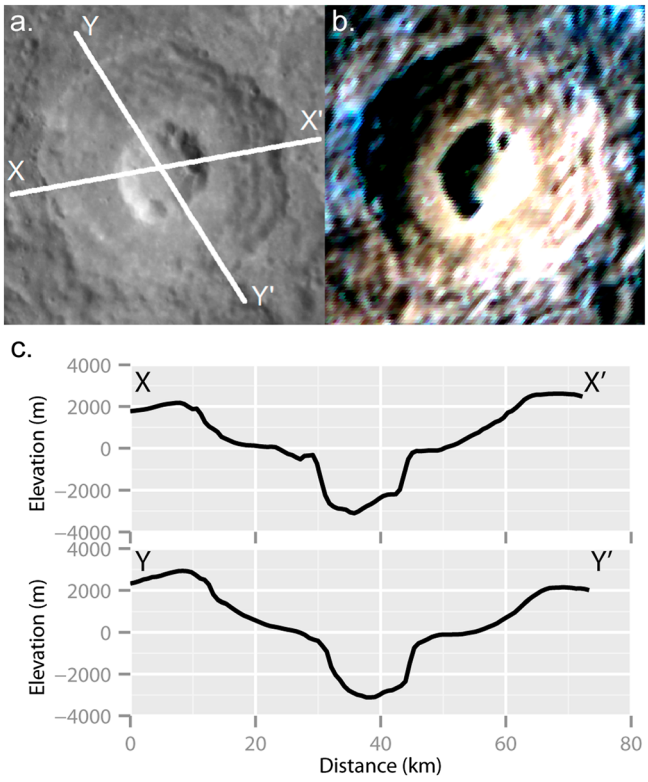

Figure 6. Pit 7038 (located at −89.3°E, −21.1°N) lies at the center of an impact crater and is surrounded by relatively bright, red deposits with little appreciable relief. (a) White lines indicate the locations of cross sections in Figure 6c. (b) A bright, red, diffuse-margined spectral anomaly is centered on the pit (composite of EW0259266820I, EW0259266840G, and EW0259266824F); (c) West-east and northwest-southeast cross sections from the DEM across the pit and crater show no pit-centered anomalous relief.

a central uplift feature would be expected but where an uplift feature is not observed or is anomalously small. This suggests that the crater was infilled by volcanic material that covered its peak structure prior to formation of the pit.

Although there is a clear spatial correlation between endogenic pits and hollows [*Thomas et al*., 2014a], we find no correlation between pit or deposit area and either proximity to hollows or the areal extent of nearby hollows.

3.2. Extent and Morphology of Pits and Deposits

3.2.1. Pits

Endogenic pits vary widely in size. The 327 individual pits at the 174 pit sites range in surface area from 1.2 to 900 km^2, with a median value of 38 km^2. The 57 pits for which we have obtained topographic data (Table S3) have calculated volumes of 1.3–1300 km^3, with a median of 40 km^3. These pits have depths of between 200 m and 4 km, with a median depth of 900 m.

The cross-sectional shape of pits varies (Figure S1). Many, especially those circumferential to the central peak of an impact crater (e.g., Figure S1b), have a V- to U-shaped cross section. Some have steep margins and relatively flat floors (e.g., Figure S1d), whereas others have morphologies intermediate between these end-members (e.g., Figure S1f). In large pits, the floor is often multileveled. This may be the result of postformational deposition of material at pit wall bases due to mass wasting, or it may be a primary feature of the pits themselves. It is probable that any pit with originally steep walls has been modified by mass wasting to some degree, so we are cautious about drawing conclusions about the mode of pit formation from the present cross-sectional shape.

In many cases, pit planform shapes are elongated along anticipated planes of weakness in impact craters, particularly around central peaks or along peak

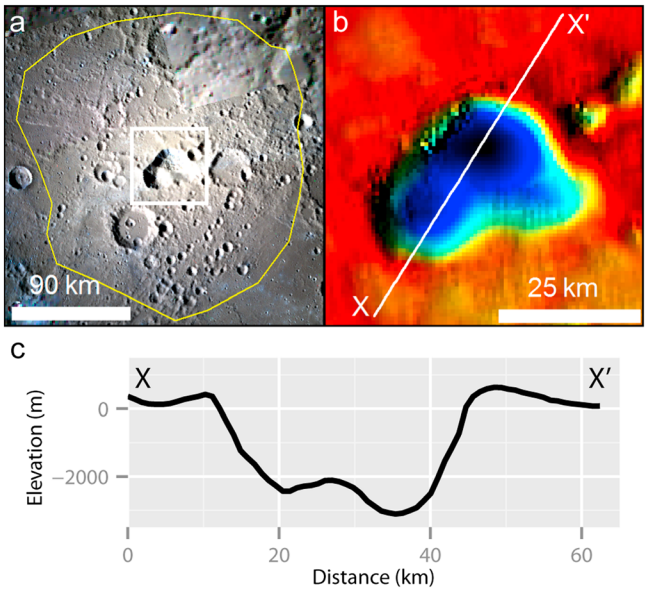

Figure 7. A large pit NE of the Rachmaninoff basin with a relatively bright and red anomaly surrounding it to considerably greater distances than those to which circumpit relief is detected. (a) A spectral anomaly (outlined in yellow) surrounds a central pit to a radius of 130 km. (b) Hillshade of the DEM in the circumpit area. White line: the southwest-northeast cross section shown in Figure 7c, illustrating the outward sloping topography at the pit rim. This pit is located at 63.9°E, 35.8°N. (The image in Figure 7a is a mosaic of color composites from frames EW0239664251I, EW0239664247G, EW0239664243F and EW0254913717I, EW0254913709G, EW0254913713F.)

rings. At some sites, several pits occur in close proximity to, or conjoined with, each other (Figure 4). Where these pits appear similarly pristine, they may have formed at the same time. However, where there are cross-cutting relationships and/or different degrees of softening of internal texture, discrete pit formation events are indicated.

3.2.2. Circumpit Deposits

The areal extent of continuous spectrally bright and red deposits around pits varies from 1.06×10^1 to 3.86×10^4 km^2 (median 5.60×10^2 km^2). They can extend to a great distance from the pit: the largest deposit, NE of the Rachmaninoff basin, has a maximum radius of 130 km. This is greater than the previously reported radius of 71 km for this deposit [*Kerber et al*., 2011] because higher-resolution color images obtained during MESSENGER's orbital campaign show that the spectral anomaly extends to greater distances. Assuming a circular deposit, the median areal extent of all the documented deposits indicates a median radius of 13.3 km.

In confirmation of earlier work [*Kerber et al*., 2011], we find that the average area of a pyroclastic deposit on Mercury is greater than that of similar lunar deposits catalogued by *Gaddis et al*. [2003] (Figure 5). Although additional candidate lunar deposits have recently been detected, these are at the low end of the range of deposit sizes on the Moon [*Gustafson et al*., 2012; *Gaddis et al*., 2013].

Where the terrain surrounding a pit is relatively flat (e.g., an impact crater floor), a relatively bright and red spectral anomaly is visible, and there is no evidence that faulting or subsequent impacts have substantially modified that topography; we attribute positive relief around the pit margins to deposition of material that originated from that pit. Our topographic data indicate such a preexisting level surface at 20 sites. Morphometric data at these sites are given in Table S3, with stereo image or MLA track product IDs indicated. Where we produced a stereo DEM, we used this to orthorectify the left image and used this as the monochrome image in figures in this section.

At six of these sites, there is little ($\leq 1°$) or no relief around the pit (Figures 6 and S2a–S2f). At all of these sites the pit is surrounded by a relatively bright and red spectral anomaly, so it appears that deposits are present, but they do not form thick accumulations close to the vents. At 12 of the remaining 14 sites, we have detected a rise around the pit (Figures 7 and S2g–S2r). The outer flank slope is usually very low: the mean of 24 measurements is $2.9 \pm 0.1°$ (standard deviation: 2.0), although the steepest is $8.3 \pm 1.1°$. The maximum elevation ranges from 29 ± 61 m to 567 ± 194 m above the surrounding topographic datum. In each case, the rise is proximal to the vent, with a mean distance from the pit margin to the slope base of 5.7 km (standard deviation: 2.8 km). The radius of the annulus of elevated terrain is usually a fraction of the entire radius of the spectral anomaly associated with the vent: the ratio between the radius of the elevated region and the radius of the spectral anomaly has a median value of 0.3. However, at two sites the relief extends as far as or even farther than the spectral anomaly. In these cases, the spectral anomaly is less pronounced than at other pit sites. At the remaining two sites, relief takes the form of a broad swell adjacent to a pit that is in turn circumferential to the center of an impact crater. The swell has a relatively bright and red

spectral signature and a rough pitted surface. The swells associated with pits 6120 and 6123 have a maximum thickness of 128 ± 61 m and 98 ± 61 m and have radii of 14 km and 8 km, respectively (Figures S2s and S2t). The bright red, rough material adjacent to Pit 6120 overlies relatively smooth, low-reflectance material (LRM), indicating that its rough surface is not the result of exposure to the normal flux of impact craters after its formation but is instead primary to the deposit.

3.2.3. Correlation of Pit and Deposit Dimensions

The area covered by spectrally red deposits generally scales with the pit area. Pits and deposits have a log-log relationship with a Pearson's product-moment correlation [*Pearson*, 1985] of 0.64 (where 1 is total positive correlation) (Figure S3). At the 13 sites where we have detected appreciable deposit topography, we found no statistically significant correlation between the extent or volume of pits and deposits and the deposit's maximum outer flank slope.

4. Discussion

Our evidence is consistent with the prevailing interpretation that the pits we catalogue here are the surface expression of volcanic vents, formed through explosive pyroclastic volcanism. Therefore, in the following discussion we will use the terms "pit" and "vent" synonymously. Our results allow us to make inferences about the style of these explosive volcanic eruptions, the physical conditions controlling them, and the mechanisms by which they form.

4.1. Eruptive Style

On Earth, explosive volcanism occurs in a number of styles: it can be steady or intermittent and it can take a number of forms depending on the ratio of juvenile magma to external water (such as seawater or groundwater) [*Wohletz and Sheridan*, 1983]. The style of eruption in turn affects the morphology of its products, so volcanic products are a window on the form(s) that explosive volcanism has taken on Mercury. As on Earth, a range of styles is to be expected both over time at a single vent and between sites of eruption.

Morphologically, Mercury's pits and deposits are most similar to maars on Earth. Maars are pits incised into bedrock that are surrounded by low-relief deposits and are underlain by a rock-filled fracture (often termed a diatreme) [*White and Ross*, 2011]. Two principle models have been advanced for maar-diatreme formation: fluidization of pyroclasts due to depressurization of a gas-rich magma [e.g., *Wilson and Head* [2007]] or phreatomagmatism (eruptions involving interaction between magma and nonmagmatic water) [*Lorenz*, 1975]. A fluidization model has been applied to explain widely dispersed glass beads on the Moon's surface, hypothesizing that the formation of a gas-rich foam at dike tips at great depths could drive short, steady eruptions [*Wilson and Head*, 2003]. It is possible that such a process occurred on Mercury, although as deposits are, on average, larger on Mercury than on the Moon, it does not necessarily follow that a similar eruption style was responsible for their formation. The hypothesis that Mercury's pits and deposits formed by a process comparable to phreatomagmatism is intriguing in light of growing evidence for near-surface volatiles on Mercury. In particular, the formation of hollows in the LRM substrate, probably primarily by sublimation, indicates that this substrate is (or was) volatile rich [*Blewett et al*., 2013; *Thomas et al*., 2014a]. Because phreatomagmatic eruptions are explosive due to the addition of external volatiles, the magma need not have had a high volatile content at depth. However, we find no correlation between the proximity or extent of nearby hollows and the scale of pyroclastic pits and deposits. Therefore, although we cannot exclude the possibility of a nonmagmatic source for some of the volatiles that drove explosive eruptions, the evidence does not at present support their playing a major part.

It is an oversimplification to draw direct comparisons between our observations of Mercury and styles of volcanism on Earth on the basis of similar deposit morphology alone. For example, Earth's atmosphere allows nonballistic transport mechanisms such as convection in an eruption column and pyroclastic flow, whereas its higher gravity reduces the ballistic range of similar-sized particles [*McGetchin et al*., 1974]. The same can be said for comparing pyroclastic landforms on Mercury with those on Mars, where air resistance reduces the ballistic range of pyroclasts of a given size, despite the planet's similar gravity [*McGetchin et al*., 1974]. This means that formation of steep-sided pyroclastic cones such as those reported in Mars' Tharsis region [*Brož and Hauber*, 2012] is not favored on Mercury, particularly at the high eruption velocities implied by our data (section 4.2), at which the effect of atmospheric drag is proportionally greater.

The Moon is the terrestrial body that is most closely analogous to Mercury in terms of atmospheric pressure and gravity, so models of the dynamics of lunar explosive eruption are potentially more appropriate for understanding those processes on Mercury. For those pyroclastic deposits on Mercury that have no topographic expression, little can be inferred about the precise style of eruption: it appears that the eruption was of low volume and/or short duration, such that no discernable topography resulted from differences in the size of particles deposited at different distances [*Wilson and Head*, 1981]. However, the finding that where there is topographic relief, it is greatest close to the pit and usually lies within a more extensive thin deposit is more revealing. Modeling of lunar pyroclastic eruptions suggests that this pattern of topography cannot occur through steady eruption of fine material but instead requires extreme particle size sorting in Strombolian eruption or high-flux steady eruption where the majority of the erupted mass forms large (10 mm–1 m) particles [*Wilson and Head*, 1981]. One or both of these eruption styles may thus have been responsible for the areally extensive pyroclastic deposits on Mercury.

The processes forming a broad rise with a pitted surface adjacent to arcuate pits 6120 and 6123 (Figures S2s and S2t) may differ from those discussed above. This nonaxisymmetric relief may have formed by effusive or clastogenic flow or by nonvertical explosive eruption. Alternatively or additionally, the pitted texture of the deposit may indicate a more complex genesis: this texture has some similarity to spectrally red pitted ground (Figure 1e), which may have formed by disruption of the surface by escaping gases [*Thomas et al*., 2014a]. Given this similarity, it is interesting to note that the deposit at pit 6120 overlies LRM, which is thought to be volatile bearing. Therefore, the unusual surface texture of these pits' deposits may be due to modification of the surface by escaping gases, which might also be responsible for their broad, raised morphologies.

Whatever the style of eruption, our findings support the occurrence of multiple phases of activity at sites of pyroclastic volcanism on Mercury. Where there are multiple or coalesced pits at one location and a clear age relationship is observed (e.g., Figure 4d [*Rothery et al*., 2014]), the locus of eruption appears to have shifted over time. Additionally, at site AP2 an underabundance of small superposed impact craters indicates resurfacing of the initial deposit by a second, thin layer after up to 300 Ma (on the basis of model ages) [*Thomas et al*., 2014b].

The morphology of pyroclastic deposits and the styles of eruption they imply do not have a simple relationship with the size of the pit or deposits. Whereas the three largest deposits, around NE Rachmaninoff (Figure 7) and N Rachmaninoff (Figure S2r), have thick deposits close to the vent indicating high-volume, high-energy eruption, the fifth largest deposit, at Pit 7038 (Figure 6), has no appreciable topographic expression, indicating that the flux and total erupted volume were not enough for edifice building. The vents are large in all three cases (among the 20 largest on the planet), but their flux and duration of activity appear to have differed substantially. Considering the wide range of eruptive styles documented at volcanoes on Earth and other planets, this should not be surprising.

The large scale of pits on Mercury, and their parallel with maar-diatreme volcanoes on Earth, raises the question of whether pyroclastic deposits on Mercury are primarily juvenile or nonjuvenile material: in maars, juvenile (magmatic) material often makes up a small proportion of the erupted mass, which is mainly material stripped from the vent walls. A recent investigation of the NE Rachmaninoff deposit indicates that its chemical composition differs from that of the surrounding surface only by a relative depletion of sulfur [*Nittler et al*., 2014]. This may indicate that the cause of the deposit's spectral character is primarily volatile loss, rather than a difference in composition from the surrounding substrate. If vent formation occurred by erosion of initially sulfur-rich country rock by a high-velocity gas, the sulfur may have been volatilized and lost or remobilized during the eruption, resulting in a deposit that is sulfur poor but nevertheless nonjuvenile. At 12 sites (indicated in Table S1) where small pits with uneven floors occur within the ejecta blanket, rim or wall of an impact crater, there is the additional possibility that the pits and surrounding deposits were not formed by pyroclastic volcanism at all but resulted from volatilization of the substrate below hotly emplaced ejecta during impact crater formation (Figure S4). The dynamics by which this process could form the observed pits and deposits are untested, however, so the degree to which impact-induced volatilization could be responsible for the sites currently interpreted as the result of explosive volcanism remains unknown. Compositional data at higher spatial resolutions than currently available, to be acquired as MESSENGER's orbit descends to lower altitudes and from the forthcoming BepiColombo mission [*Fraser et al*., 2010; *Rothery et al*., 2010], may further constrain the composition of Mercury's bright, red deposits and allow distinctions to be drawn between deposits formed by different processes.

4.2. Structural Controls on Eruption

The siting of 92% of vents with pyroclastic deposits close to thrust faults and zones of weakness in impact craters strongly suggests that such structures favor the occurrence of explosive volcanism. In the context of a state of global contraction persisting over much of Mercury's history that likely inhibited magma ascent, tectonic and impact structures represent the paths of least resistance to the surface, so these zones of weakness may act as conduits.

The occurrence of explosive volcanism within impact craters and concentrated around the rim of large impact basins raises the possibility that this volcanism was triggered by the impact process, as has been suggested for the widespread smooth plains emplaced during and shortly after the Late Heavy Bombardment period of Mercury [*Marchi et al*., 2013]. However, impact-induced volcanism is controversial [*Ivanov and Melosh*, 2003; *Roberts and Barnouin*, 2012], and in any case this process has been suggested only for the largest basin-forming impacts [*Elkins-Tanton et al*., 2004]. The smallest crater that hosts a vent is 7.6 km in diameter, and the total population (121) of craters hosting vents has a median diameter of 67 km. For this scale of crater, impact-induced volcanism is improbable. Additionally, the timing of explosive volcanism around basins is not consistent with the basin-forming event triggering that volcanism. The vents around the Caloris Basin postdate the basin fill, which appears to be significantly younger than the basin itself [*Fassett et al*., 2012]. Moreover, the incision of pits into relatively young, well-preserved craters around the putative ancient basin b54 indicates that explosive volcanism in that region occurred long after the basin formed. However, it is feasible that crater formation facilitated ascent of magma by "resetting" the compressive stress in the overlying rock. Kuniyoshi, the youngest crater that hosts pyroclastic volcanism identified in our survey, may illustrate this process: it lies within a cluster of volcanic vents at the west of basin b54, where the structures delineating the basin and its constituent rings may well have permitted magma ascent from depth. Future work to constrain the relative ages of craters and basins and the explosive volcanic vents incising them will allow us to characterize this process.

If paths of crustal weakness acted as conduits for magma ascent and eruption, then the ease of access to the surface through these pathways presumably affects the volcanic style. Our results support this inference. Eleven of the 14 sites at which the buildup of detectable deposits implies relatively long lived eruption are spatially associated with likely deep seated structures. Four pits with circumpit relief lie at the center of impact craters, and one overlies the expected location of the buried peak ring within Lermontov basin. In these cases, fractures associated with uplifted central peaks and peak rings could have facilitated magma ascent. RS-03 (in SW Caloris) and other nearby vents incise a network of wrinkle ridges and, additionally, lie along a line radial to the center of the Caloris Basin. The formation of the vents, as well as where they formed, may have been structurally controlled [*Rothery et al*., 2014].

4.3. Mechanisms of Eruption

The eruption styles indicated by variations in pyroclastic deposit morphology, the evidence for a tectonic control on eruption, and the large scale of some such deposits together shed light on the mechanisms that have resulted in explosive volcanic eruptions on Mercury for much of its geological history despite a thickening lithosphere in a state of net contraction.

The colocation of clusters of explosive volcanic vents along major fold and thrust belts [*Byrne et al*., 2014] and around large impact basins suggests that the presence of deep-seated faults and fractures facilitates magma rise from depth. At smaller scales, near-surface faults and fractures may have allowed eruption from shallow magma sources.

Magma storage at shallow levels is implied by three strands of evidence: the horizontal scale of the deposits, the eruption style suggested by the deposit morphology, and the occurrence of repeated eruption at the same location. The horizontal scale of the deposits is controlled by the kinetic energy of particle ejection, which in turn is approximately proportional to the volatile mass fraction in the released magma [*Wilson*, 1980]. Mercury's pyroclastic deposits are, on average, larger than those on the Moon, despite the higher gravitational acceleration on Mercury, and so a higher volatile content is required to distribute particles to a given distance. This indicates a higher average volatile concentration in pyroclastic eruptions on Mercury than on the Moon. The maximum distance, X, to

which particles can be ejected on an airless body can be related to the initial ejection velocity, v, by the relation

$$X = \frac{v^2}{g} \sin 2\theta, \quad (1)$$

where g is gravitational acceleration (3.7 m/s^2 on Mercury) and θ is the angle at which dispersal is greatest (45°). This relationship indicates that for the largest deposit, NE Rachmaninoff, the farthermost particles (those 130 km from the vent) were ejected at a minimum velocity of ~690 m/s. If we follow the method of *Wilson et al*. [2014] and make the simplifying assumptions that the gas expands adiabatically and that the pyroclasts acquire all of the gas speed, we can determine the released magmatic volatile gas fraction, n, by

$$n = \frac{(v^2 m(\gamma - 1))}{2QT\gamma}, \quad (2)$$

where m is the molecular mass of the gas, γ is the ratio of the heat capacity of the gas at constant pressure and at constant volume, Q is the universal gas constant, and T is the magmatic temperature. At a magmatic temperature of 1750 K, where γ for CO is 1.302 [*Hilsenrath*, 1955], equation (2) indicates that the emplacement of pyroclasts to radial distances of 130 km from the vent requires over 10 wt % CO if this were the sole volatile species. The corresponding values for CO_2 (γ = 1.116 at 1500 K [*Hilsenrath*, 1955]) and H_2O (γ = 1.25 at 1600 K [*Wilson et al*., 2014]) are approximately 7.5 wt % and 6 wt %, respectively. For comparison, melt inclusions indicate that basaltic magmas on Earth have up to 0.7 wt % CO_2 and 1.2–6 wt % H_2O [*Metrich and Wallace*, 2008]. The highest H_2O contents are in subduction settings, where processes occur that are unlikely to be comparable to those on Mercury. In nonarc settings, the H_2O content is considerably lower. At Kilauea in Hawaii, for example, magmatic gas contents responsible for fire-fountaining eruptions have been calculated as 0.3 wt % H_2O, 0.3 wt % CO_2, and 0.1 wt % S [*Greenland et al*., 1985]. These values are substantially lower than those required to emplace pyroclasts around the NE Rachmaninoff vent but are similar to values needed to form pyroclastic deposits of the median radius on Mercury, 13.3 km: 1.1 wt % CO, 0.8 wt % CO_2, or 0.6 wt % H_2O. In reality, a combination of more reduced species is to be expected in Mercury's magmas. Chemical equilibrium models suggest that N_2, CO, S_2, CS_2, S_2Cl, Cl, Cl_2, and COS could be the most abundant volatiles in Hermean melts [*Zolotov*, 2011], and the finding that the NE Rachmaninoff deposit is low in sulfur supports the involvement of one or more sulfur-bearing species [*Nittler et al*., 2014]. All of these volatiles have a higher molecular mass than CO, and so unless γ at magmatic temperatures is substantially lower than that of CO, a concentration greater than 10 wt % is required to deposit pyroclasts up to 130 km from a vent. As we do not find support for an external source of these species (section 4.1), a high volatile fraction suggests either a high intrinsic volatile content in the magma or concentration of volatiles prior to eruption.

The formation of hollows by sublimation [*Blewett et al*., 2013; *Thomas et al*., 2014a] and the detection of volatile elements on Mercury's surface [*Nittler et al*., 2011; *Peplowski et al*., 2011] imply that the planet has a higher bulk volatile content than previously thought [e.g., *Cameron* [1985]]. In order to attain a volatile content in excess of that present in basalts on Earth, however, further concentration of volatiles prior to eruption is probably required. On Earth, it is observed that volatile oversaturation occurs through fractional crystallization in magmas stored at shallow crustal levels [*Tait et al*., 1989; *Fowler and Spera*, 2008]. Indeed, it has been suggested that the buildup of overpressure through this process is a necessary condition for eruption from such a chamber [*Tait et al*., 1989]. Notably, the occurrence of several pits at one location is also consistent with shallow subsurface storage. Although it is possible that these pits were formed by magmas erupting from the tips of multiple dikes that propagated from considerable depth, the close spatial relationships of these depressions is more consistent with having originated from a single location in the shallow subsurface.

The styles of explosive volcanism we infer for the majority of the sites where we have topographic data are also consistent with shallow magma storage. If, as predicted by models for lunar explosive volcanism [*Wilson and Head*, 1981], the deposits with circumpit relief on Mercury formed by Strombolian eruption, or steady eruption of predominantly large particles, this is indicative of bubble coalescence prior to eruption. Bubbles coalesce when magma rise is slow relative to bubble rise velocity, as when ascending magma slows or stalls. At those other sites where pyroclastic deposits have little topographic expression, a low-volume,

short-duration eruption is probable. Although it has been suggested that such deposits can form as a result of volatile concentration in a dike tip propagating from depth [*Wilson and Head*, 2003], overpressurization of a magma reservoir prior to failure could also lead to an eruption scenario that, because it is cyclical, is more consistent with the observed occurrence of several pits at a single site.

Where magma stalls at shallow crustal levels and accumulates volatiles, preexisting near-surface faults and fractures can play a controlling role on eruption. Numerical modeling indicates that if large overlying subvertical fractures are present, dike propagation may occur along these even if the distribution of stress due to neutral buoyancy would favor horizontal dike propagation in their absence [*Parfitt et al*., 1993]. These fractures can act as valves: brittle failure occurs when magma exceeds the frictional strength of the faults, volatiles and/or magma is released, and then the fractures/faults seal again after the driving stress falls below that strength [*Sibson et al*., 1988]. If the magma chamber is a closed system, these processes will lead to repeated cycles of pressurization and eruption. This process accounts for the high volatile content and limited eruption volume we have inferred for many of Mercury's pyroclastic deposits, as well as the evidence for multiple eruptions at a single location.

Roof failure may occur above a magma reservoir even without the presence of preexisting fractures, if the chamber is shallow enough and a sufficiently thick layer of low-density foam accumulates in its upper part [*Parfitt et al*., 1993]. Such a scenario may explain the occurrence of vents incised into effusive deposits within impact craters. Initial volcanism in these craters would have been facilitated by the presence of subsurface faults and fractures produced by crater formation, enabling sufficiently efficient magma rise for effusive eruption, or high-flux explosive eruption with clastogenic flow. When a resistant cap of lava had accumulated on the crater floor, magma ascent would have been inhibited, and volatiles would accumulate prior to eruption so that later eruptions were more explosive. This progression in the ease of magma ascent may be responsible for pits clustered around the margins of the lava-filled Caloris Basin.

The association of subsurface magma storage and explosive eruption due to volatile overpressure raises the possibility, originally noted by *Gillis-Davis et al*. [2009], that Mercury's pits form by collapse into magma reservoirs. Their model suggested magma withdrawal at depth, but at the 150 sites where pyroclastic deposits are observed, subsidence could alternatively have resulted from magma chamber drainage during eruption, as for the formation of large calderas during explosive volcanism on Earth. On Earth, the cross-sectional shape of a collapse caldera is the result of its eruptive history, the presence of preexisting faults or the prevailing stress field, the dimensions of the magma chamber, and postformational mass wasting. Nonetheless, the end-member morphologies observed on Earth encompass the range observed on Mercury [*Cole et al*., 2005]. Until more compositional data for Mercury's pyroclastic deposits are available, we cannot definitively assess the degree to which subsidence and the stripping of wall rock (section 4.1) contribute to pit formation. In either case, however, it is probable that preexisting faults such as those associated with impact crater central uplifts play some role in the siting and morphology of the resulting pit.

We therefore conclude that for any location on the surface of Mercury, the potential for explosive volcanism and its scale and periodicity is strongly controlled by the presence or absence of both deep-seated and surficial faults and fractures. These zones of weakness assume such a key role on Mercury due to the planet being in a tectonic regime of net compression and the absence of other controlling conditions, such as the plate tectonics of Earth and the high-loading stresses resulting from the density contrast between highlands and mare on the Moon [*Head and Wilson*, 1992; *McGovern and Litherland*, 2011].

5. Conclusions

We have identified 174 sites where endogenic pits occur on Mercury, at 150 of which they are surrounded by deposits that are likely pyroclastic in nature. There are multiple pits at 64 of these sites (with a total of 327 pits in all), suggesting multiple episodes and/or loci of eruption in close proximity to each other. The areal extent of pyroclastic deposits suggests a greater concentration of volatiles driving these eruptions than for lunar explosive volcanism and similar to, or higher than, that associated with basaltic pyroclastic eruptions on Earth. This unexpectedly high volatile content may in part be a result of concentration of magmatic volatiles in shallow magma chambers, and so the scale of the deposits does not necessarily correspond to the bulk volatile content of the planet. Nevertheless, the sizes and abundance of these deposits support the growing viewpoint that Mercury's interior is far more enriched in volatile species than had been thought.

Pyroclastic landforms are, in general, widely distributed across the planet, but they are conspicuously absent in the thicker parts of smooth volcanic plains. We find strong support for the hypothesis that impact crater-related fractures and thrust faults control the occurrence of explosive volcanism, with deep-seated structures allowing magma ascent from depth and surficial faults and fractures controlling ascent, and possibly acting as valves for magma and/or volatile release, from shallow magma reservoirs. We therefore suggest that explosive eruption on Mercury represents an interaction between impact cratering, magma fractionation, and tectonic deformation that has allowed ascent and eruption of magma over a substantial part of the planet's geological history.

Acknowledgments

The image and laser altimetry data used in this paper are available at the PDS Geosciences Node of Washington University, St. Louis, USA. All other data are provided in Tables S1–S3 or available from the authors on request. Rebecca Thomas acknowledges a PhD studentship from the Science and Technology Facilities Council (UK) (ST/K502212/1). David Rothery acknowledges support from UKSA PP/E002412/1 and ST/M002101/1 and STFC ST/L000776/1. We thank Sebastien Besse and Paul Byrne for their helpful and insightful reviews of the manuscript.

References

Banks, M. E., C. Klimczak, Z. Xiao, T. R. Watters, R. G. Strom, S. E. Braden, C. R. Chapman, S. C. Solomon, and P. K. Byrne (2014), Duration of activity on lobate-scarp thrust faults on Mercury, *45th Lunar Planet Sci. Conf.*, *2722*, doi:10.1029/2003GL019171.

Benz, W., A. Anic, J. Horner, and J. A. Whitby (2007), The origin of Mercury, *Space Sci. Rev.*, *132*(2–4), 189–202, doi:10.1007/s11214-007-9284-1.

Blewett, D. T., et al. (2011), Hollows on Mercury: MESSENGER evidence for geologically recent volatile-related activity, *Science*, *333*(6051), 1856–1859, doi:10.1126/science.1211681.

Blewett, D. T., et al. (2013), Mercury's hollows: Constraints on formation and composition from analysis of geological setting and spectral reflectance, *J. Geophys. Res. Planets*, *118*, 1013–1032, doi:10.1029/2012JE004174.

Brož, P., and E. Hauber (2012), A unique volcanic field in Tharsis, Mars: Pyroclastic cones as evidence for explosive eruptions, *Icarus*, *218*(1), 88–99, doi:10.1016/j.icarus.2011.11.030.

Byrne, P. K., C. Klimczak, A. M. C. Şengör, S. C. Solomon, T. R. Watters, and S. A. Hauck (2014), Mercury's global contraction much greater than earlier estimates, *Nat. Geosci.*, *7*(April), 301–307, doi:10.1038/NGEO2097.

Cameron, A. G. W. (1985), The partial volatilization of Mercury, *Icarus*, *64*(2), 285–294, doi:10.1016/0019-1035(85)90204-0.

Cavanaugh, J. F., J. C. Smith, X. Sun, A. E. Bartels, L. Ramos-Izquierdo, D. J. Krebs, and J. F. McGarry (2007), The Mercury Laser Altimeter instrument for the MESSENGER mission, *Space Sci. Rev.*, *131*(1–4), 451–479, doi:10.1007/s11214-007-9273-4.

Cole, J., D. Milner, and K. Spinks (2005), Calderas and caldera structures: A review, *Earth Sci. Rev.*, *69*(1–2), 1–26, doi:10.1016/j.earscirev.2004.06.004.

Denevi, B. W., et al. (2009), The evolution of Mercury's crust: A global perspective from MESSENGER, *Science*, *324*(5927), 613–8, doi:10.1126/science.1172226.

Denevi, B. W., et al. (2013), The distribution and origin of smooth plains on Mercury, *J. Geophys. Res. Planets*, *118*, 891–907, doi:10.1002/jgre.20075.

Elkins-Tanton, L. T., B. H. Hager, and T. L. Grove (2004), Magmatic effects of the lunar late heavy bombardment, *Earth Planet. Sci. Lett.*, *222*(1), 17–27, doi:10.1016/j.epsl.2004.02.017.

Fassett, C. I., et al. (2012), Large impact basins on Mercury: Global distribution, characteristics, and modification history from MESSENGER orbital data, *J. Geophys. Res.*, *117*, E00L08, doi:10.1029/2012JE004154.

Fegley, B., and A. G. W. Cameron (1987), A vaporization model for iron/silicate fractionation in the Mercury protoplanet, *Earth Planet. Sci. Lett.*, *82*, 207–222.

Fowler, S. J., and F. J. Spera (2008), Phase equilibria trigger for explosive volcanic eruptions, *Geophys. Res. Lett.*, *35*, L08309, doi:10.1029/2008GL033665.

Fraser, G. W., et al. (2010), The mercury imaging X-ray spectrometer (MIXS) on BepiColombo, *Planet. Space Sci.*, *58*(1–2), 79–95, doi:10.1016/j.pss.2009.05.004.

Gaddis, L. R., M. I. Staid, J. A. Tyburczy, B. R. Hawke, and N. E. Petro (2003), Compositional analyses of lunar pyroclastic deposits, *Icarus*, *161*(2), 262–280, doi:10.1016/S0019-1035(02)00036-2.

Gaddis, L. R., L. Weller, J. Barrett, R. Kirk, M. Milazzo, J. Laura, B. R. Hawke, T. Giguere, B. Horgan, and K. Bennett (2013), "New" volcanic feature in lunar, floor-fractured Oppenheimer crater, *Lunar Planet. Inst. Sci. Conf.*, *44*, 2262.

Gillis-Davis, J. J., D. T. Blewett, R. W. Gaskell, B. W. Denevi, M. S. Robinson, R. G. Strom, S. C. Solomon, and A. L. Sprague (2009), Pit-floor craters on Mercury: Evidence of near-surface igneous activity, *Earth Planet. Sci. Lett.*, *285*(3–4), 243–250, doi:10.1016/j.epsl.2009.05.023.

Goudge, T. A., et al. (2014), Global inventory and characterization of pyroclastic deposits on Mercury: New insights into pyroclastic activity from MESSENGER orbital data, *J. Geophys. Res. Planets*, *119*, 635–658, doi:10.1002/2013JE004480.

Greenland, L. P., W. I. Rose, and J. B. Stokes (1985), An estimate of gas emissions and magmatic gas content from Kilauea volcano, *Geochim. Cosmochim. Acta*, *49*(1), 125–129.

Gustafson, J. O., J. F. Bell, L. R. Gaddis, B. R. Hawke, and T. A. Giguere (2012), Characterization of previously unidentified lunar pyroclastic deposits using Lunar Reconnaissance Orbiter Camera data, *J. Geophys. Res.*, *117*, E00H25, doi:10.1029/2011JE003893.

Hawkins, S. E., et al. (2007), The Mercury Dual Imaging System on the MESSENGER spacecraft, *Space Sci. Rev.*, *131*(1–4), 247–338, doi:10.1007/s11214-007-9266-3.

Head, J. W., and L. Wilson (1992), Lunar mare volcanism: Stratigraphy, eruption conditions, and the evolution of secondary crusts, *Geochim. Cosmochim. Acta*, *56*, 2155–2175.

Head, J. W., et al. (2008), Volcanism on Mercury: Evidence from the First MESSENGER flyby, *Science*, *80*(321), 69–72, doi:10.1016/j.icarus.2008.04.018.

Hilsenrath, J. (1955), *Tables of Thermal Properties of Gases: Comprising Tables of Thermodynamic And Transport Properties of Air, Argon, Carbon Dioxide, Carbon Monoxide, Hydrogen, Nitrogen, Oxygen, And Steam*, U.S. Dep. of Commerce, National Bureau of Statistics, Washington.

Ivanov, B. A., and H. J. Melosh (2003), Impacts do not initiate volcanic eruptions: Eruptions close to the crater, *Geology*, *31*(10), 869, doi:10.1130/G19669.1.

Jenness, J. (2011), Tools for graphics and shapes: Extension for ArcGIS, Jenness Enterp.

Kerber, L., J. W. Head, S. C. Solomon, S. L. Murchie, D. T. Blewett, and L. Wilson (2009), Explosive volcanic eruptions on Mercury: Eruption conditions, magma volatile content, and implications for interior volatile abundances, *Earth Planet. Sci. Lett.*, *285*(3–4), 263–271, doi:10.1016/j.epsl.2009.04.037.

Kerber, L., J. W. Head, D. T. Blewett, S. C. Solomon, L. Wilson, S. L. Murchie, M. S. Robinson, B. W. Denevi, and D. L. Domingue (2011), The global distribution of pyroclastic deposits on Mercury: The view from MESSENGER flybys 1–3, *Planet. Space Sci.*, *59*(15), 1895–1909, doi:10.1016/j.pss.2011.03.020.

Kerber, L., S. Besse, J. W. Head, D. T. Blewett, T. A. Goudge, and P. Jussieu (2014), The global distribution of pyroclastic deposits on Mercury: The view from orbit, *45th Lunar and Planetary Science Conference*, 2862.
Lorenz, B. V. (1975), Formation of phreatomagmatic maar-diatreme volcanoes and its relevance to kimberlite diatremes, *Phys. Chem. Earth*, *9*, 17–27.
Marchi, S., C. R. Chapman, C. I. Fassett, J. W. Head, W. F. Bottke, and R. G. Strom (2013), Global resurfacing of Mercury 4.0–4.1 billion years ago by heavy bombardment and volcanism, *Nature*, *499*(7456), 59–61, doi:10.1038/nature12280.
McGetchin, T. R., M. Settle, and B. A. Chouet (1974), Cinder cone growth modeled after Northeast Crater, Mount Etna, Sicily, *J. Geophys. Res.*, *79*(23), 3257–3272, doi:10.1029/JB079i023p03257.
McGovern, P. J., and M. M. Litherland (2011), Lithospheric stress and basaltic magma ascent on the Moon, with implications for large volcanic provinces and edifices, *42nd Lunar Planet. Sci. Conf.*, *2587*, doi:10.1038/NGEO897.
Metrich, N., and P. J. Wallace (2008), Volatile abundances in basaltic magmas and their degassing paths tracked by melt inclusions, *Rev. Mineral. Geochem.*, *69*(1), 363–402, doi:10.2138/rmg.2008.69.10.
Moran, P. A. P. (1950), Notes on continuous stochastic phenomena, *Biometrika*, *37*(1–2), 17–23.
Moratto, S. Z. M., M. J. Broxton, R. A. Beyer, M. Lundy, and K. Husmann (2010), Ames Stereo Pipeline, NASA's open source automated stereogrammetry, *Lunar Planet. Sci. Conf.*, *41*, 2364.
Nittler, L. R., et al. (2011), The major-element composition of Mercury's surface from MESSENGER X-ray spectrometry, *Science*, *333*(6051), 1847–1850, doi:10.1126/science.1211567.
Nittler, L. R., et al. (2014), Sulfur-depleted composition of Mercury's largest pyroclastic deposit: Implications for explosive volcanism and surface reflectance on the innermost planet, *Lunar Planet. Sci. Conf.*, *45*, 1391.
Parfitt, E. A., L. Wilson, and J. W. Head (1993), Basaltic magma reservoirs: Factors controlling their rupture characteristics and evolution, *J. Volcanol. Geotherm. Res.*, *55*(1–2), 1–14, doi:10.1016/0377-0273(93)90086-7.
Pearson, K. (1985), Notes on regression and inheritance in the case of two parents, *Proc. R. Soc. London*, *58*, 240–242.
Peplowski, P. N., et al. (2011), Radioactive elements on Mercury's surface from MESSENGER: Implications for the planet's formation and evolution, *Science*, *333*, 1850–1852, doi:10.1126/science.1211576.
Roberts, J. H., and O. S. Barnouin (2012), The effect of the Caloris impact on the mantle dynamics and volcanism of Mercury, *J. Geophys. Res.*, *117*, E02007, doi:10.1029/2011JE003876.
Rothery, D. A., R. J. Thomas, and L. Kerber (2014), Prolonged eruptive history of a compound volcano on Mercury: Volcanic and tectonic implications, *Earth Planet. Sci. Lett.*, *385*, 59–67.
Rothery, D., et al. (2010), Mercury's surface and composition to be studied by BepiColombo, *Planet. Space Sci.*, *58*(1–2), 21–39, doi:10.1016/j.pss.2008.09.001.
Schultz, R. A. (2000), Localization of bedding plane slip and backthrust faults above blind thrust faults: Keys to wrinkle ridge structure, *J. Geophys. Res.*, *105*(E5), 12,035–12,052, doi:10.1029/1999JE001212.
Sibson, R. H., F. Robert, and K. H. Poulsen (1988), High-angle reverse faults, fluid-pressure cycling, and mesothermal gold-quartz deposits, *Geology*, *16*, 551–555.
Strom, R. G., N. J. Trask, and J. E. Guest (1975), Tectonism and volcanism on Mercury, *J. Geophys. Res.*, *80*(17), 2478–2507, doi:10.1029/JB080i017p02478.
Tait, S., C. Jaupart, and S. Vergniolle (1989), Pressure, gas content and eruption periodicity of a shallow, crystallising magma chamber, *Earth Planet. Sci. Lett.*, *92*, 107–123.
Thomas, R. J., D. A. Rothery, S. J. Conway, and M. Anand (2014a), Hollows on Mercury: Materials and mechanisms involved in their formation, *Icarus*, *229*, 221–235, doi:10.1016/j.icarus.2013.11.018.
Thomas, R. J., D. A. Rothery, S. J. Conway, and M. Anand (2014b), Long-lived explosive volcanism on Mercury, *Geophys. Res. Lett.*, *44*, doi:10.1002/2014GL061224.
Watters, T. R., S. C. Solomon, M. S. Robinson, J. W. Head, S. L. André, S. A. Hauck, and S. L. Murchie (2009), The tectonics of Mercury: The view after MESSENGER's first flyby, *Earth Planet. Sci. Lett.*, *285*(3–4), 283–296, doi:10.1016/j.epsl.2009.01.025.
Wetherill, G. W. (1988), Accumulation of Mercury from planetesimals, in *Mercury*, edited by F. Vilas, C. R. Chapman, and M. Matthews, pp. 670–691, Univ. of Arizona Press, Tucson, Ariz.
White, J. D. L., and P.-S. Ross (2011), Maar-diatreme volcanoes: A review, *J. Volcanol. Geotherm. Res.*, *201*(1–4), 1–29, doi:10.1016/j.jvolgeores.2011.01.010.
Wilson, L. (1980), Relationships between pressure, volatile content and ejecta velocity in three types of volcanic explosion, *J. Volcanol. Geotherm. Res.*, *8*, 297–313.
Wilson, L., and J. W. Head (1981), Ascent and eruption of basaltic magma on the Earth and Moon, *J. Geophys. Res.*, *86*(B4), 2971–3001, doi:10.1029/JB086iB04p02971.
Wilson, L., and J. W. Head (2003), Deep generation of magmatic gas on the Moon and implications for pyroclastic eruptions, *Geophys. Res. Lett.*, *30*(12), 1605, doi:10.1029/2002GL016082.
Wilson, L., and J. W. Head (2007), An integrated model of kimberlite ascent and eruption, *Nature*, *447*(7140), 53–57, doi:10.1038/nature05692.
Wilson, L., J. W. Head, and A. R. Tye (2014), Lunar regional pyroclastic deposits: Evidence for eruption from dikes emplaced into the near-surface crust, *Lunar Planet. Sci. Conf.*, *45*, 1223.
Wohletz, K. H., and M. F. Sheridan (1983), Hydrovolcanic explosions II. Evolution of basaltic tuff rings and tuff cones, *Am. J. Sci.*, *283*, 385–413.
Zolotov, M. Y. (2011), On the chemistry of mantle and magmatic volatiles on Mercury, *Icarus*, *212*(1), 24–41, doi:10.1016/j.icarus.2010.12.014.
Zuber, M. T., et al. (2012), Topography of the northern hemisphere of Mercury from MESSENGER laser altimetry, *Science*, *336*, 217–220.

Erratum

In the originally published version of this article, the "Spectral anomaly" column of Table S1 contained incorrect values. These have since been corrected and this version may be considered the authoritative version of record.